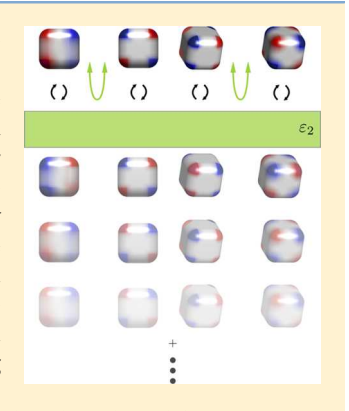
# Multipolar Nanocube Plasmon Mode-Mixing in Finite Substrates

Charles Cherqui, †,|| Guoliang Li,‡,|| Jacob A. Busche,†,|| Steven C. Quillin,† Jon P. Camden,\*,§,⊥o and David I. Masiello\*,†

ABSTRACT: Facile control of the radiative and nonradiative properties of plasmonic nanostructures is of practical importance to a wide range of applications in the biological, chemical, optical, information, and energy sciences. For example, the ability to easily tune not only the plasmon spectrum but also the degree of coupling to light and/or heat, quality factor, and optical mode volume would aid the performance and function of nanophotonic devices and molecular sensors that rely upon plasmonic elements to confine and manipulate light at nanoscopic dimensions. While many routes exist to tune these properties, identifying new approaches—especially when they are simple to apply experimentally—is an important task. Here, we demonstrate the significant and underappreciated effects that substrate thickness and dielectric composition can have upon plasmon hybridization as well as downstream properties that depend upon this hybridization. We find that even substrates as thin as ~10 nm can nontrivially mix free-space plasmon modes, imparting bright character to those that are dark (and vice versa) and, thereby, modifying the plasmonic density of states as well as the system's near- and far-field optical properties.



A combination of electron energy-loss spectroscopy (EELS) experiment, numerical simulation, and analytical modeling is used to elucidate this behavior in the finite substrate-induced mixing of dipole, quadrupole, and octupole corner-localized plasmon resonances of individual silver nanocubes.

ue to their ability to capture and convert light into intense, nanoscopic surface-bound electric fields, localized surface plasmons (LSPs) in noble metal nanostructures are currently the focus of a vigorous worldwide research effort. 1-8 The high sensitivity of LSPs to subtle changes in their host environment make them excellent candidates for a wide range of biological, 9-12 chemical, 13-16 and optical sensing applications, 17and their giant absorption cross sections 20,21 and extraordinarily small mode volumes<sup>22-24</sup> hold great promise in future photovoltaic and nanophotonic devices.<sup>2,25-3</sup>

Past theoretical studies have addressed the interaction of plasmonic nanoparticles with both homogeneous dielectric environments<sup>31–33</sup> and semi-infinite substrates,<sup>34–39</sup> but only few<sup>37,40</sup> have explicitly accounted for the influence of the latter upon higher-order LSP modes. Effects of substrates of finite thickness are even more unexplored, as doing so is computationally demanding<sup>41</sup> and experimental data is lacking due to the weak coupling of higher-order LSP modes to the radiation field. Electron energy-loss spectroscopy (EELS), performed in a scanning transmission electron microscope (STEM), offers a route to overcome this challenge by using fast electrons as a probe of matter instead of light. Due to its high degree of spatial confinement and broad spectral range, STEM/EELS can access the complete plasmonic response (i.e., collective electronic excitations of both surface and bulk character), providing detailed spatial and spectral information on the influence of the substrate's dielectric properties and thickness upon the full plasmonic spectrum. This was clearly demonstrated in 2015 when Li et al.<sup>39</sup> used STEM/EELS to characterize the complete surface and bulk plasmon responses of truncated silver nanospheres ranging from 20–1000 nm in diameter on semi-infinite substrates.

While having played an important role in the discovery and early understanding of the surface and bulk plasmon, 42,43 the past decade has witnessed a renaissance in the application of fast electron spectroscopy to plasmonic nanoparticles and their assemblies. 44-46 Unlike in optical spectroscopies where supporting substrates can be millimeters thick and well-approximated as semi-infinite, typical substrates in STEM-based electron spectroscopies must be thin enough to allow the electrons to pass through and reach the EEL detector. This requirement translates to substrates on the order of 1–100 nm, thicknesses comparable to the plasmonic specimens themselves. In this regime, substrate effects can be surprisingly nontrivial and distinctly different from semi-infinite substrates, uniform background environments, and vacuum, motivating the need for careful study.

Electrodynamics dictates that each plasmon mode (here referred to as a multipole) will interact and hybridize with its own image as well as with those of all other plasmon multipoles through the

Received: December 11, 2017 Accepted: January 9, 2018 Published: January 9, 2018

Department of Chemistry, University of Washington, Seattle, Washington 98195, United States

<sup>&</sup>lt;sup>‡</sup>Center for Electron Microscopy, Institute for New Energy Materials & Low-Carbon Technologies, School of Materials Science and Engineering, Tianjin University of Technology, Tianjin 300384, China

<sup>§</sup>Department of Chemistry and Biochemistry, University of Notre Dame, Notre Dame, Indiana 46556, United States

<sup>&</sup>lt;sup>1</sup>Department of Materials Science and Engineering, University of Tennessee, Knoxville, Tennessee 37996, United States

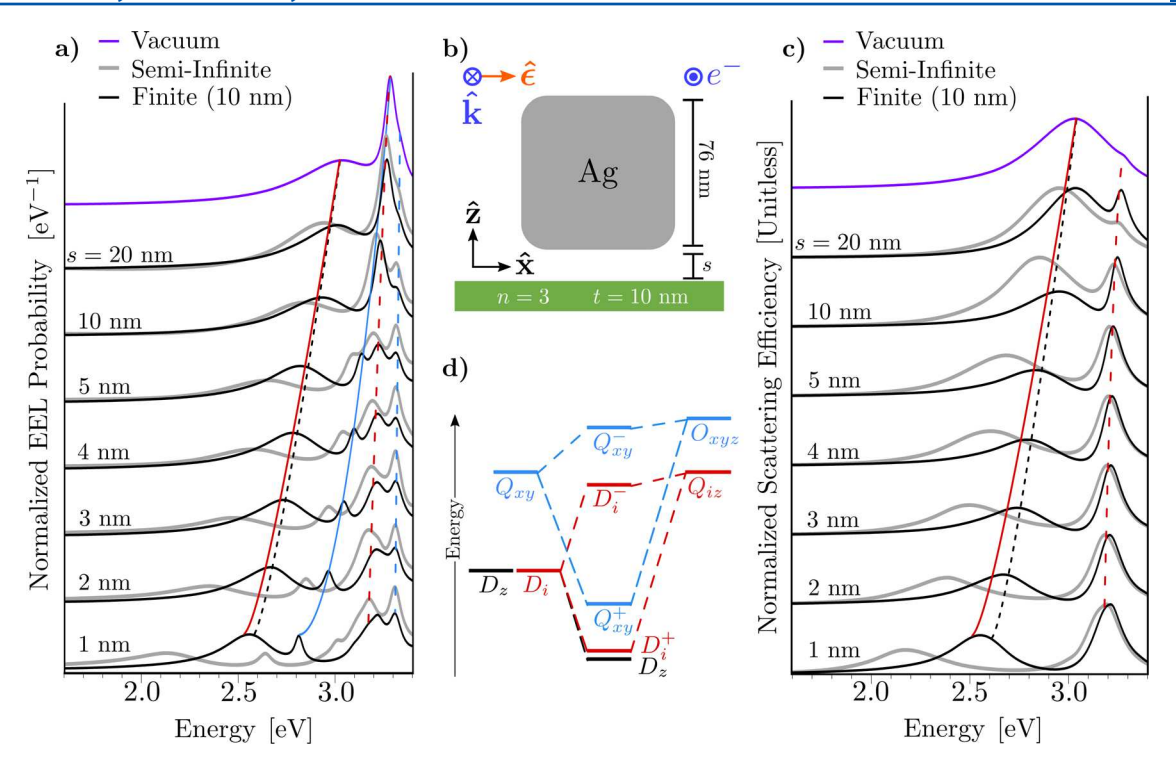


**Figure 1.** Computed evolution of nanocube LSP mode mixing versus separation distance in a substrate of refractive index n = 3 and thickness t = 10 nm. (a) Aloof EEL and (c) optical scattering spectra showing the progression of the nanocube's free-space dipolar  $(D_{xy}, D_z)$ , quadrupolar  $(Q_{xyy}, Q_{xz})$ , and octupolar  $(Q_{xyz})$  modes with substrate-separation distance s interacting through either finite (black) or semi-infinite (gray) substrates. The vertical curves are provided only as a guide to the eye. An illustration of the system is shown in panel (b) together with a schematic of the finite-substrate-induced hybridization diagram in panel (d). The y-oriented LSP modes  $D_y$  and  $Q_{yz}$  are not indicated explicitly since they are degenerate with those oriented in the x-direction. Of the five hybridized modes displayed, all are evident in the EEL spectrum, while only those that are bright (red) are accessible via optical scattering. Note that significant LSP mode mixing occurs even on substrates as thin 10 nm in thickness.

substrate. It is often assumed that only dielectric composition, i.e., refractive index, affects this image hybridization and that otherwise all substrates behave nearly identically, independent of thickness. It might also be expected that thin substrates, i.e., those that are of the same thickness as the plasmonic target specimens or thinner, would resemble vacuum and have little influence upon the LSP resonances, leaving each LSP mode essentially unhybridized. Surprisingly, however, neither presumption is true.

Here we demonstrate the nontrivial impact that substrates of finite thickness (t) and varying refractive index (n) have upon LSP + image LSP mode mixing in individual silver nanocubes using monochromated and aberration-corrected STEM/EELS experiment combined with full-wave numerical electrodynamics simulations of the fast electron probe. Further analytical modeling serves as a basis to qualitatively and even semiquantitatively expose the relevant hybridization physics. Most interesting is the "hall of mirrors" image effect produced uniquely by finite substrates, <sup>47</sup> which, depending upon *t*, *n*, and the particle–substrate separation distance s, can mix LSPs in such a way that significant hybridization occurs even with substrate thicknesses well below 100 nm. Figure 1 compares the evolution of the optical scattering spectrum of a silver nanocube with s at fixed t and n to that of EELS, which is a near-field probe of extinction (i.e., the sum of absorption and scattering). 44-46 In the following we will show that varying these parameters provides an opportunity to control the degree of LSP hybridization, even for higher-order modes beyond the usual dipole and quadrupole LSP resonances. 37,48-50 Taken together, the presented work provides a new pathway to understand and exploit plasmon mode mixing to employ even intrinsically dark plasmons for nano-optical applications.

Nanocubes, in particular, have recently garnered significant attention \$^{51,52}\$ due to the localization of their low-lying LSP modes to the cube's corners. Each so-called corner mode can either be dark or bright depending on the mode's coupling efficiency to the radiation field. The high degree of curvature at the corners induces exceptionally strong electric near-fields there, leading to stronger LSP-environment coupling than in other nanoparticle shapes (e.g., spheres and rods). For this reason, nanocubes make an excellent platform for careful investigation of finite-substrate effects.

It is well-known that the performance of nanocube-based sensors can be furthered enhanced via substrate interactions. For example, their free-space dipole LSP modes parallel to the substrate can mix with free-space quadrupole modes<sup>37,48-50</sup> to produce hybridized surface charge oscillations that take on the same asymmetric character of the environment, i.e., with effective dipolar surface charge distributions localized toward (proximal) and away (distal) from the substrate. When excited by light, these hybridized modes can be made to interfere and produce Fano antiresonances in the scattering spectrum,<sup>37</sup> which have been successfully implemented for use in asymmetric color routing, 53,54 ultrafast spontaneous emission,<sup>55</sup> and a variety of solar light harvesting applications. 40,56,57 For example, Li et al. 40 used STEM/EELS to image the flow of energy between the proximal LSP modes of individual nanocubes and excitonic transitions in their supporting semiconductor substrates with nanoscopic precision, demonstrating that environmental transitions can be resonantly tuned to enhance plasmonic energy transfer. 58,59

As demonstrated in Figure 1 and shown schematically in Figure 2a, the symmetry of the nanocube dictates that the only distinct corner-localized free-space charge distributions are the

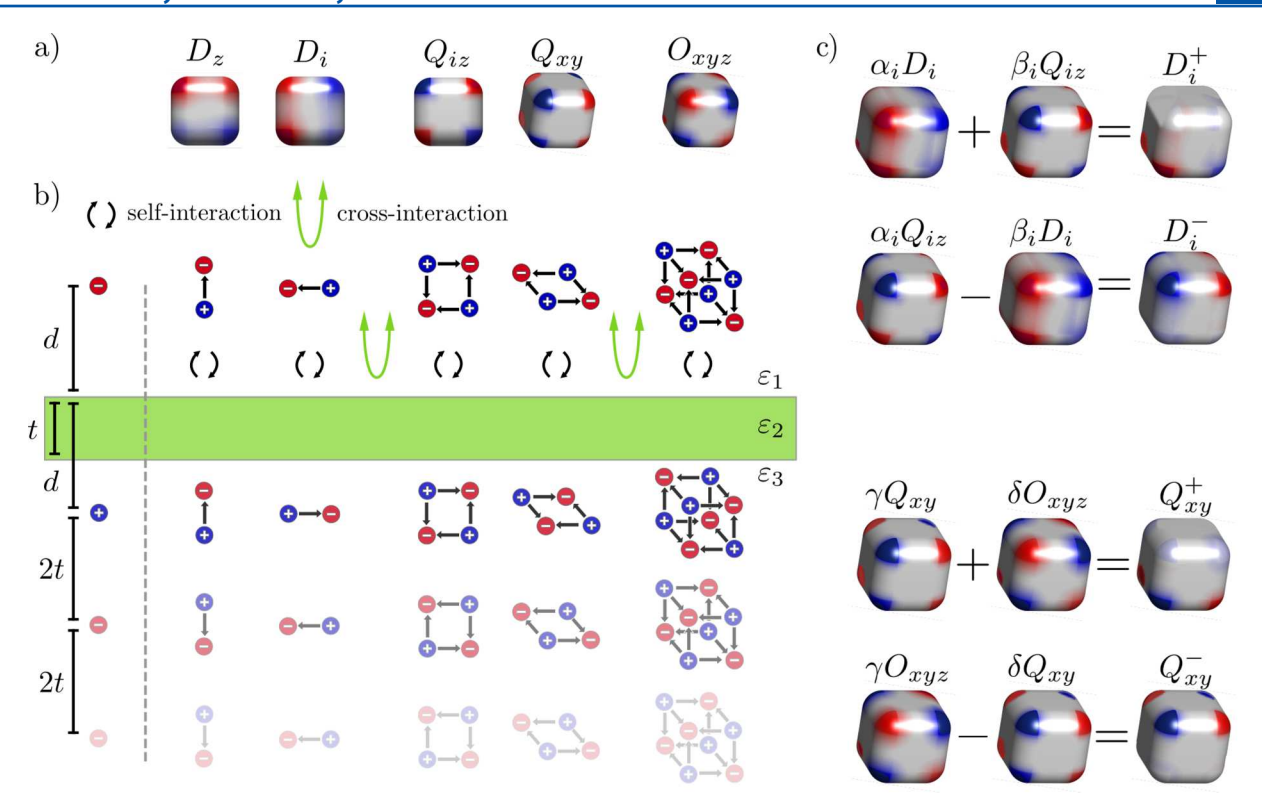


Figure 2. (a) Computed quasistatic surface charge distributions of the lowest-lying five nondegenerate free space LSP corner modes of the nanocube. Explicitly shown are the triply degenerate  $D_z$  and  $D_v$  and  $Q_{xy}$  modes ( $i \in \{x,y\}$ ), as well as the single corner octupole mode  $O_{xyz}$ . (b) Schematic of the image response of a finite substrate to these LSP modes, with the interaction between source and image organized into "self-interactions", represented by black arrows, and "cross-interactions", represented by green arrows. The relative phase between successive image multipoles is determined by the particular values of the dielectric constants  $\varepsilon_1$ ,  $\varepsilon_2$ , and  $\varepsilon_3$ ; the configuration shown here corresponds to  $\varepsilon_2 > \varepsilon_1 = \varepsilon_3$ . (c) Computed mixing of the nanocube's free space LSP modes into substrate-dressed, hybridized LSP modes. The in-phase and out-of-phase modes  $D_i^+$  and  $D_i^-$  are linear combinations of the bright  $D_i$  and the dark  $Q_{iz}$  modes. The former (latter) has a dipolar surface charge distribution localized to the corners proximal (distal) to the substrate. The in-phase and out-of-phase modes  $Q_{xy}^+$  and  $Q_{xy}^-$  are linear combinations of the dark modes  $Q_{xy}$  and  $Q_{xyz}$ . The former (latter) has a quadrupolar surface charge distribution localized to the corners proximal (distal) to the substrate.

triply degenerate dipole  $(D_x, D_y, D_z)$  and quadrupole  $(Q_{xy}, Q_{xz})$  $Q_{vz}$ ) modes as well as the single octupole mode,  $O_{xyz}$ . All other LSP modes involve some amount of surface charge localized at the edges and/or faces of the structure and are of higher energy and are ignored in the following. We approximate each nanocube corner mode as a pure Cartesian multipole, associating the two via their respective surface charge distributions.<sup>60</sup> Within a finite substrate, each LSP multipole induces an infinite collection of images of itself as illustrated in Figure 2b. These images, in turn, act back on the LSP, allowing each LSP to couple to its own images (self-interactions) as well as to those of other LSPs (cross-interactions). The relative orientation between the free space modes and their images determines the selection rules: each mode interacts with its own image, but only the two pairwise cross-interactions between  $D_i$  and  $Q_{iz}$  and  $Q_{xy}$  and  $O_{xyz}$ , with  $i \in \{x, y\}$ , are allowed.

All self- and cross-interaction strengths are determined from the electrostatic image response

$$\Phi_{\text{ind}}(\mathbf{x}) = -\frac{q_0'}{\varepsilon_1 |\mathbf{x} - \mathbf{r}_0'|} + \sum_{j=1}^{\infty} \frac{q_j'}{\varepsilon_1 |\mathbf{x} - \mathbf{r}_j'|} \quad \text{(for } z > 0\text{)}$$
(1)

of a finite substrate of thickness t to a point charge q located a distance d from the top layer in the z-direction. Despite its complicated form, eq 1 has a simple interpretation, which is illustrated in the first column of Figure 2b. The first term is nothing more

than the image potential of the semi-infinite substrate with image charge  $q'_0 = \Delta_{21}q$  located at  $\mathbf{r}'_0 = (0, 0, -d)$ . The second term accounts for the finiteness of the substrate and is a sum over the potentials of image charges  $q'_j = \Delta_{23}[1-\Delta_{21}^2](\Delta_{21}\Delta_{23})^{j-1}q$  located at  $\mathbf{r}'_j = (0, 0, -d-2jt)$ , with j a nonzero integer. The strength of all image charges is proportional to the surface jump condition  $\Delta_{ab} = (\varepsilon_a - \varepsilon_b)/(\varepsilon_a + \varepsilon_b)$  with  $a, b \in \{1, 2, 3\}$ . As displayed in Figure 2b,  $\varepsilon_1$  is the dielectric constant in the upper half space,  $\varepsilon_2$  is the dielectric constant of the finite substrate, and  $\varepsilon_3$  is the dielectric constant in the lower half space, with  $n_a = \sqrt{\varepsilon_a} \cdot t$  can be larger or smaller than d, however, we note that  $\Phi_{\rm ind} \to -q'_0/\varepsilon_1 |\mathbf{x}-\mathbf{r}'_0|$  as  $t\to\infty$  and  $\Phi_{\rm ind}\to0$  as  $t\to0$ .

Based on the image potential in eq 1, an LSP Hamiltonian  $^{45,60}$  can be written with  $\Phi_{\rm ind}$  parametrizing the substrate-mediated multipolar LSP–LSP interaction energies (see Methods). Its diagonalization produces the amplitudes of the hybridized modes of the interacting nanocube—substrate system

$$D_{i}^{+} = \alpha_{i}D_{i} + \beta_{i}Q_{iz}$$

$$D_{i}^{-} = \alpha_{i}Q_{iz} - \beta_{i}D_{i}$$

$$D_{z} = D_{z}$$

$$Q_{xy}^{+} = \gamma Q_{xy} + \delta Q_{xyz}$$

$$Q_{xy}^{-} = \gamma Q_{xyz} - \delta Q_{xy}$$
(2)

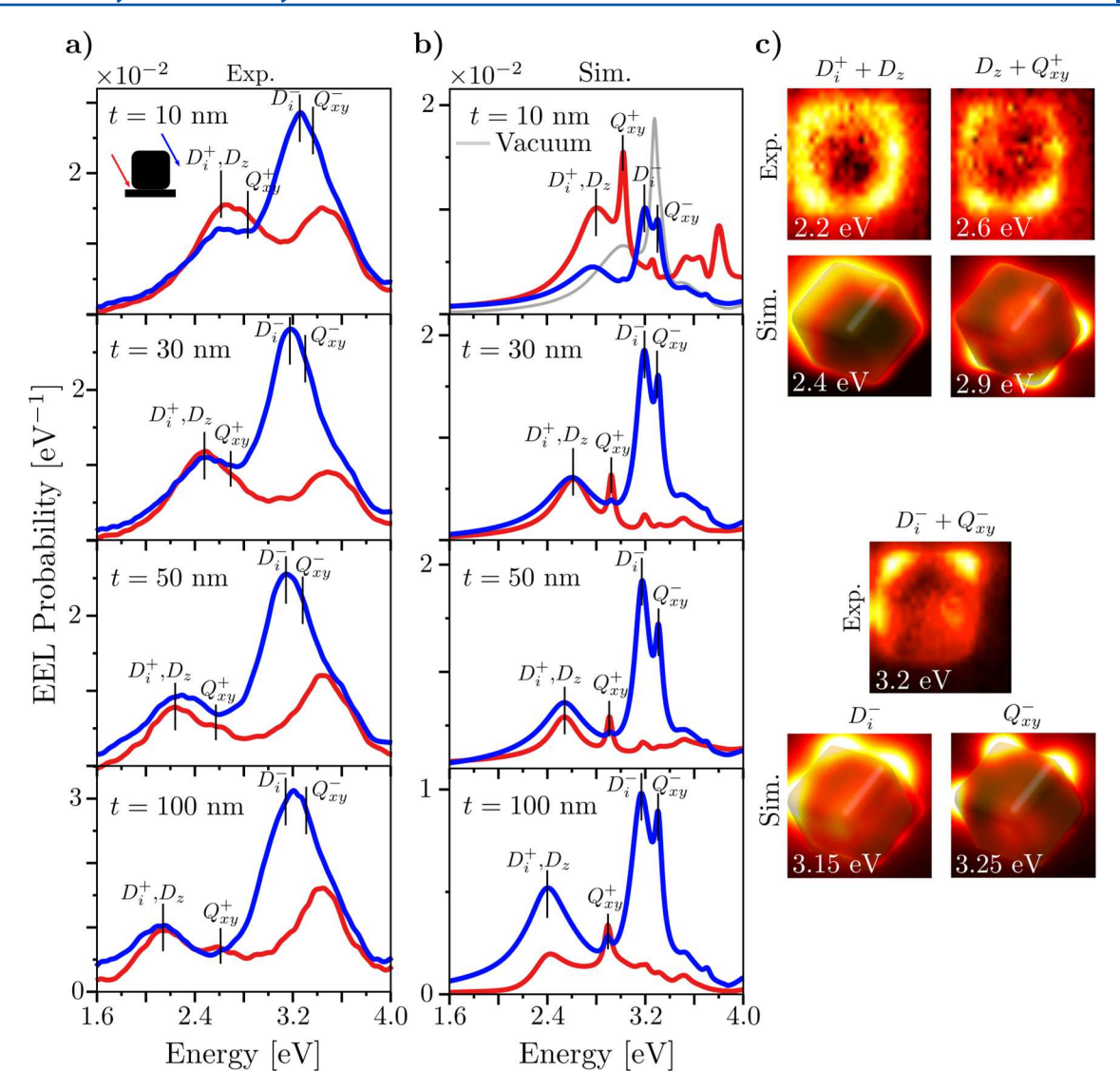


**Figure 3.** Experimental (a) and simulated (b) point spectra for tilted 76 nm nanocubes supported by t=10, 30, 50, and 100 nm  $\mathrm{SiN}_x$  substrates with  $n_{\mathrm{SiN}_x}=2.1$ . EEL spectra are acquired at two aloof beam positions: one at a distal corner of the cube (blue) and the other at a proximal corner (red). In each panel, the spectral position of each LSP mode is estimated from the model. (c) Experimental and simulated EEL mode maps corresponding to the resonance energies in the EEL spectra for the t=100 nm  $\mathrm{SiN}_x$  substrate. The upper panels correspond to superpositions of the substrate-localized  $D_i^+$  and  $Q_{xy}^+$  modes, and the  $D_z$  mode. The lower panels show an experimental EEL mode map that is a superposition of  $D_i^-$  and  $Q_{xy}^-$  alongside EEL maps of the same modes individually resolved via simulation.

as well as their natural frequencies

$$\begin{split} &\Omega_{i}^{+} = \sqrt{\alpha_{i}^{2}(\omega_{i}^{2} - f_{i}) + \beta_{i}^{2}(\omega_{iz}^{2} - f_{iz}) - g_{i}\alpha\beta_{i}} \\ &\Omega_{i}^{-} = \sqrt{\alpha_{i}^{2}(\omega_{iz}^{2} - f_{iz}) + \beta_{i}^{2}(\omega_{i}^{2} - f_{i}) + g_{i}\alpha\beta_{i}} \\ &\Omega_{z} = \sqrt{\omega_{z}^{2} - f_{z}} \\ &\Omega_{xy}^{+} = \sqrt{\gamma^{2}(\omega_{xy}^{2} - f_{xy}) + \delta^{2}(\omega_{xyz}^{2} - f_{xyz}) - g_{xy}\gamma\delta} \\ &\Omega_{xy}^{-} = \sqrt{\gamma^{2}(\omega_{xyz}^{2} - f_{xyz}) + \delta^{2}(\omega_{xyz}^{2} - f_{xy}) + g_{xy}\gamma\delta} \end{split}$$

$$(3)$$

with  $i \in \{x, y\}$ . Here,  $\alpha_{i\nu}$   $\beta_{i\nu}$   $\delta$ , and  $\gamma$  are expansion coefficients derived from eq 1 and indicate that the degree of mode mixing and corresponding amount of surface charge localization increases with increasing t or  $\varepsilon_2$ . Explicitly, these expansion coefficients are defined as  $\alpha_i = \cos \theta_i$ ,  $\beta_i = \sin \theta_i$ ,  $\gamma = \cos \theta_{xv}$ 

and  $\delta=\sin\theta_{xy}$  where  $\tan2\theta_i=g_i/(\omega_{iz}^2-\omega_i^2+f_i-f_{iz})$  and  $\tan2\theta_{xy}=g_{xy}/(\omega_{xyz}^2-\omega_{xy}^2+f_{xy}-f_{xyz})$ . Figure 2c (upper panel) shows that the surface charge distributions resulting from interaction among  $D_i$  and  $Q_{iz}$  are effective substrate- and vacuumlocalized hybridized LSP modes of dipolar character, labeled as  $D_i^+$  and  $D_i^-$  for  $i \in \{x, y\}$ , while coupling among  $Q_{xy}$  and  $O_{xyz}$ (bottom panel, Figure 2c) leads to effective substrate- and vacuum-localized quadrupole modes, labeled as  $Q_{xy}^+$  and  $Q_{xy}^-$ Interestingly, due to its symmetry,  $D_z$  does not efficiently interact with any LSP multipole other than itself. Nonetheless, the spatial profile of its field is substrate-localized as the in-phase, collinear arrangement of the dipole and image dipoles within the selfhybridized mode induces a capacitive junction, biasing the field profile downward in the upper half plane; while counterintuitive, this means that the EEL profile of the  $D_z$  mode is vacuum localized as the probability to excite this in-phase arrangement of dipoles is largest immediately above the cube and falls to zero in the junction. The cross- and self-interaction coupling constants *g* 

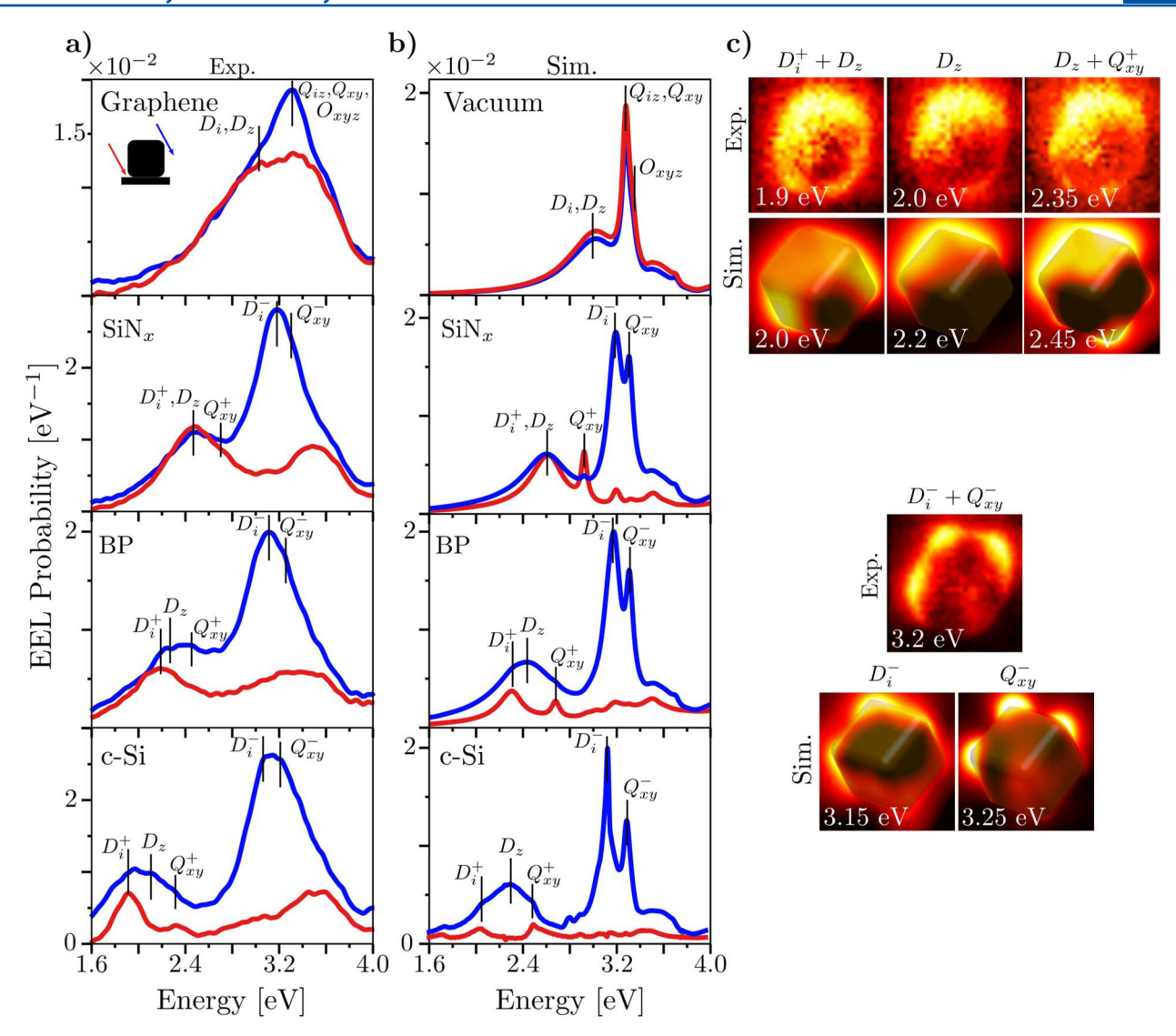


Figure 4. Experimental (a) and simulated (b) point spectra for tilted 76 nm nanocubes supported on single layer graphene (modeled as vacuum in simulation), t = 30 nm SiN<sub>x</sub>, t = 30 nm BP, and t = 35 nm c-Si. The system is excited at two electron beam positions, one at a distal corner (blue) and the other at a proximal corner (red) of the nanocube. In each panel, the spectral position of each LSP mode is estimated from the model. (c) Experimental and simulated EEL maps for the peaks found in the spectra of the t = 35 nm c-Si nanocube—substrate system. The upper panels correspond to a superposition of the substrate-localized  $D_i^+$  and  $Q_{xy}^+$  modes with the vacuum-localized  $D_z^-$  mode, as well as the isolated vacuum-localized  $D_z^-$  mode. The lower panels display an experimental EEL map corresponding to a superposition of  $D_i^-$  and  $Q_{xy}^-$  alongside maps of the same modes individually resolved in simulation.

and f are determined from the interaction energy of the  $(l, m)^{\text{th}}$  multipole with the induced potential of the  $(l', m')^{\text{th}}$  image multipole, i.e.,  $\int d^3x \rho_{lm}(\mathbf{x}) \Phi^{\text{ind}}_{l'm'}(\mathbf{x})$ , and dictate the substrate-induced mode-mixing experienced by the uncoupled, free-space corner modes of natural frequency  $\omega_{i\nu}$   $\omega_{z\nu}$   $\omega_{iz\nu}$   $\omega_{xy\nu}$  and  $\omega_{xyz}$ . Further details of the model can be found in the Methods Section as well as in ref 60.

Figure 3a shows experimental STEM/EELS point spectra for individual  $76 \pm 5$  nm wide silver nanocubes with  $13 \pm 1$  nm corner radii, supported on  $\mathrm{SiN}_x$  substrates with t = 10, 20, 30, and 100 nm. Figure 3b shows analogous simulated STEM/EELS spectra for a 76 nm wide silver nanocube with 12.5 nm corner radii supported on an identical set of substrates. In both experiment and simulation, the entire system is first tilted and then excited using an aloof electron beam positioned at a distal corner (blue) and at a proximal corner (red) of the cube. At t = 10 nm ( $n_{\mathrm{SiN}} = 2.1$ ), mode mixing is weak but, surprisingly, not negligible.

As t increases, so too does the strength of the interaction between nanocube and substrate, leading to a pronounced red-shifting of the proximal  $D_i^+$  modes. As dictated by eqs 1-3, their energy is lowered twice: once by self-interaction, and again by cross-interaction. Conversely, these two effects compete—with the self-interaction red-shifting and the cross-interaction blue-shifting the resonance position—to cause a relatively small energetic shift in the distal  $D_i^-$  modes relative to  $Q_{iz}$ . Indeed, simulations show a slight red-shift; however, limitations in the resolution of the experiment ( $\approx 200 \text{ meV}$ ) and presence of the nearby  $Q_{xy}^-$  mode make its independent spectral identification challenging. Nevertheless, a small red-shift in the superposition of  $D_i^-$  and  $Q_{xy}^-$  peaks (Figure 3a) is experimentally observed in the t=10-30 nm data.

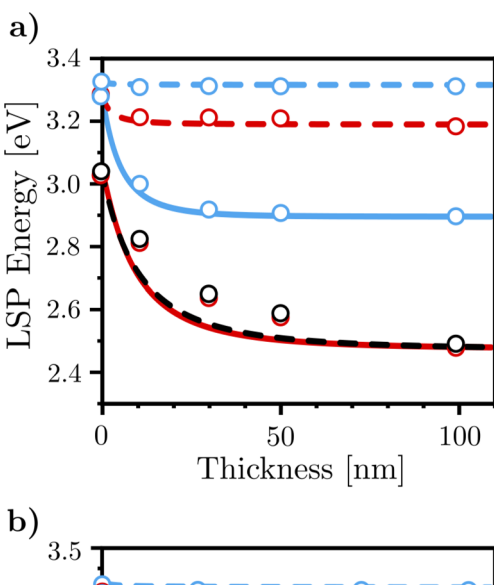
Due to its symmetry, the remaining quadrupolar corner mode  $Q_{xy}$  does not interact with any of the three dipole modes nor any other quadrupole mode. Its substrate-induced localization, therefore, must be generated by interaction with the image of the octupole mode  $O_{xyz}$  in addition to its own. These couplings lead

to a significantly red-shifted  $Q_{xy}^+$  in comparison to  $Q_{xy}$ , and a slightly red-shifted  $Q_{xy}^-$  in comparison to  $O_{xyz}$ ; the reasons for these energy shifts are identical to those explained previously for the  $D_i^{\pm}$  modes. Figure 3a,b shows the appearance of the  $Q_{xy}^{+}$  peak only in the proximal beam position (red). In the simulations (b), this occurs at t = 30 nm, while, in experiment (a) it occurs at t = 50 nm. Again the vacuum-localized  $Q_{xy}^-$  mode can clearly be seen in all simulated spectra for all substrate thicknesses considered, but limitations in energy resolution cause both the  $Q_{xy}^-$  and  $D_i^-$  to appear as a single  $\sim$ 3.2 eV peak in the data. In both experiment and theory,  $Q_{xy}^-$  and  $D_i^-$  are identified as vacuumlocalized since they are only significantly excited from the distal beam position. The (lack of) evolution of these modes with substrate thickness is representative of the more general behavior that higher-order LSP modes quickly saturate to a final energy due to the competing effects of self- and cross-interactions as well as the more rapid falloff of the electric fields.

EEL probability maps for the nanocube on a  $t=100~\rm nm~SiN_x$  substrate are shown in Figure 3c for all five distinct hybridized modes. In the upper panel, we see that, because  $D_z$  does not hybridize with any other LSP mode, it retains its spectrally bright, free-space character, causing its broad resonance profile to overlap with both  $Q_{xy}^+$  and  $D_i^+$ . Thus,  $D_z$  appears as a background signal and only superpositions of  $D_z$  with  $D_i^+$  and  $Q_{xy}^+$  can be measured. Easier to resolve in both experiment and simulation and shown in the lower panel of Figure 3c is the vacuum localization expected of the  $D_i^-$  and  $Q_{xy}^-$  modes. Again, as for the data presented in Figure 3, limitations in experimental resolution means that  $D_i^-$  and  $Q_{xy}^-$  can only be measured simultaneously in experiment, but individually in simulations.

The experimental and simulated data presented in Figure 4 demonstrate that, as predicted by eqs 1–3, mode hybridization can be controlled either by changing the substrate's thickness or dielectric composition. To explore the remainder of this parameter space, individual  $76 \pm 2$  nm nanocubes are prepared on four different dielectric substrates and excited under the same conditions described above. Rather than vary substrate thickness, EEL spectra are collected for both proximal and distal beam positions for individual nanocubes deposited on (i) single layer graphene (modeled as vacuum in simulation), (ii) t = 30 nm silicon nitride (SiN<sub>x</sub>,  $n_{\text{SiN}_x} = 2.1$ ), (iii) t = 30 nm boron phosphide (BP,  $n_{\text{BP}} = 3$ ), and (iv) t = 35 nm crystalline silicon (c-Si,  $n_{\text{c-Si}} = 3.7$ ). As expected, the spectra presented in Figure 4 exhibit a spectral evolution similar to what was shown previously in Figure 3 where substrate thickness was increased at constant composition.

In examining eq 1, it is evident that maximum coupling occurs when the first term dominates over the second. As described previously, this is the limit of the semi-infinite substrate. However, independent of t, the same qualitative behavior can be attained by increasing the substrate's dielectric constant, as  $q_i' \to 0 \ (j \ge 1)$  when  $\varepsilon_2 \gg \varepsilon_1$ . In this limit, the maximum amount of mode mixing is determined by the jump condition  $\Delta_{21} = (\varepsilon_2 - \varepsilon_1)/(\varepsilon_2 + \varepsilon_1)$ . Figure 5 highlights the symmetry between increasing t and increasing  $\varepsilon_2$ . The strength of each LSP + image LSP interaction is comparably magnified as the substrate's polarizability is increased, either by an addition of dielectric material (t) or an increase to the permittivity of the existing substrate ( $\varepsilon_2$ ). Surprisingly, substrates composed of high dielectric materials such as c-Si can more strongly mix LSP modes at t = 35 nm than a t = 100 nm SiN<sub>x</sub> substrate can. This is most clearly evident in the experimental and simulated EEL mode maps of the c-Si nanocube-substrate system displayed in



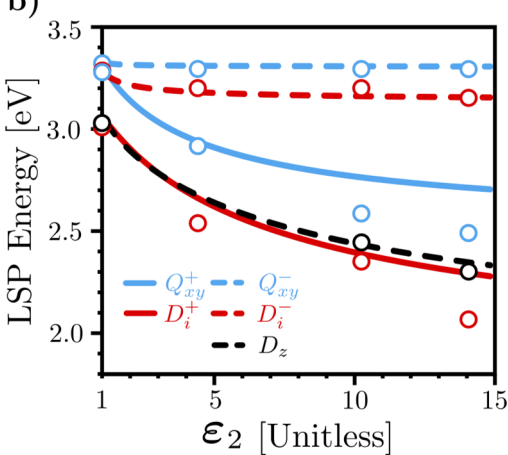


Figure 5. Spectral evolution of the nanocube's lowest-lying five nondegenerate corner-localized LSP modes versus (a) substrate thickness and (b) substrate dielectric constant. In both panels, the bullets correspond to the simulated resonance peak positions, and the lines correspond to the energies predicted by the model. Quantitative disagreements between the two arise because the projection of the spherical plasmon modes onto the basis of the cube with rounded corners is approximate and because the simulations are fully retarded while the model is derived in the quasistatic limit; the latter approximates the interaction between each LSP and the higher-order images, which fall off more quickly with t than would be predicted by the full field. Nonetheless, both display the same symmetry between increasing dielectric constant and thickness. The t values in panel (a) and  $\varepsilon_2$  values in panel (b) span the full range of substrate thicknesses and refractive indices considered in our reported experimental data. Panel (a) uses the SiN<sub>x</sub> dielectric constant value  $\varepsilon_{SiN_x}$  = 4.41, while panel (b) uses the same experimental substrate thicknesses from Figure 4b for single-layer graphene (t = 0 nm,  $\varepsilon_g = 1$ ), SiN<sub>x</sub> (t = 30 nm,  $\varepsilon_{SiN_x} = 4.41$ ), BP (t = 30 nm,  $\varepsilon_{BP} = 10$ ), and c-Si (t = 35 nm,  $\varepsilon_{c-Si} = 13.7$ ). In comparing both panels, it is evident that thinner substrates of higher index can mix LSP modes equally as efficiently as thicker substrates of lower

Figure 4c. The high value of  $\varepsilon_2$  produces a significant enough splitting that the vacuum-localized  $D_z$  mode can be isolated in between  $D_i^+$  and  $Q_{xy}^+$ . As predicted by the model, the competing nature of self- and cross-interactions dictates that the lower-energy member of a hybridized pair can continue to red-shift until  $\Delta_{21} \sim 1$ , eliminating the second term in eq 1 and maximizing the associated image response. This implies that  $D_i^+$  and  $Q_{xy}^+$  have the most potential for application, as they can

conveniently be tuned across a wide range of frequencies simply by adjusting substrate thickness and/or refractive index.

In conclusion, we have combined STEM/EELS experiment with numerical simulation and analytical modeling to elucidate the behavior of plasmon mode mixing in substrates of finite thickness. Substrate-induced hybridization of the seven lowestlying LSP modes of individual silver nanocubes are investigated, with both the spectral and spatial behavior of their hybridization imaged by the fast electron probe. Varying substrate thickness from 10-100 nm at constant refractive index as well as varying substrate refractive index from 1-4 at constant thickness reveals that substrates as thin as 10 nm can significantly mix free-space LSP modes, imparting bright character to initially dark LSPs and vice versa, thereby strongly modifying the radiative and nonradiative properties of the resulting hybridized modes. The surprising fact that substrate thickness matters and can be readily changed in the laboratory has far-reaching impact across a wide range of applications.

## METHODS

STEM/EELS Experiments. EEL spectra were acquired in a monochromated Carl Zeiss Libra 200MC (S)TEM operated with an accelerating voltage of 200 kV. Each spectrum acquisition was executed with a collection semiangle of 12 mrad, a convergence semiangle of 9 mrad, and a dispersion of 29 meV per channel. Energy resolution, defined as the full width at half-maximum of the zero-loss peak, for each acquisition is 150 meV with the electron beam probing only the substrate. For each nanocube, EEL spectrum images responsible for producing LSP mode maps were collected by defining a pixelated region of interest around the particle, where 1 pixel is  $\sim$ 4 × 4 nm².

Experimentally obtained EEL mode maps are analyzed using the Gatan Digital Micrograph software. Such maps are generated by removing the background using the reflected-tail model and normalized to the total spectral area. LSP mode maps were prepared by plotting spectral intensities from energy slices in which the peak maxima of the distal/proximal point spectra are located.

Substrate and Nanocube Preparation. The 10, 30, 50, and 100 nm thick silicon nitride membranes were purchased from Norcada Inc. The part numbers are NT050Z, NT050X, NT050A, and NT050C, respectively. All of the silicon membranes were synthesized via lower-pressure chemical vapor deposition (LPCVD). They have the same refractive indices according to the specification sheet from the company. The single-layer graphene substrate was purchased from Ted Pella Inc. The part number is 21710-5. The crystalline silicon substrate was purchased from the TEMwindows Company. The part number is US100-C35Q33. The crystalline boron phosphide substrate was prepared by milling a boron phosphide thin film with a focused ion beam (FIB). The thickness was calculated by applying the log-ratio method to an EELS spectrum of the substrate. The calculation was performed using the Gatan DigitalMicrograph software. The silver nanocubes were purchased from NanoComposix Inc. The part number is DSS1572. All samples used in the EELS experiments were prepared by dropcasting the nanocubes onto the substrates and then letting the water solution dry.

LSP + Image LSP Hybridization Model. Details of rigorously mapping the solutions of Maxwell's equations in the quasistatic limit onto a multipolar LSP Hamiltonian can be found in ref 45. Each spherical free-space LSP oscillator inherits an effective mass  $m_{lm}$  and natural frequency  $\omega_{lm}$ , defined completely in terms of the plasma frequency as well as its multipole number (l, m),

high-frequency and background dielectric functions  $\varepsilon_{\infty}$  and  $\varepsilon_b$ , and radius a. To model the nanocube, we scale the effective mass and resonance frequency of each spherical LSP mode to reproduce the analogous free-space nanocube LSP mode in EELS. The (corner) LSP masses of the nanocube are in general lighter than those of the nanosphere, implying that the nanocube is more polarizable than the nanosphere.

Important to this work is the interaction Hamiltonian

$$H_{\text{int}} = \frac{1}{2} \sum_{lm,l'm'} \int d^3x \rho_{lm}(\mathbf{x}) \Phi_{l'm'}^{\text{ind}}(\mathbf{x})$$
(4)

describing the coupling between LSP modes as mediated by the image response of the substrate. Here

$$\rho_{lm}(\mathbf{x}) = eQ_{lm}a^{l-1}\frac{(-)^{l+1}}{(l+2)!}Y_{lm}(\theta,\phi)\left(\frac{\partial}{\partial r}\right)^{l+2}\delta(r)$$
(5)

is the charge density of the (l, m)<sup>th</sup> LSP multipole located at the origin and

$$\Phi_{l'm'}^{\text{ind}}(\mathbf{x}) = \int d^3x' G_{\text{ind}}(\mathbf{x}, \mathbf{x}') \rho_{l'm'}(\mathbf{x}')$$
(6)

with Poisson Green function  $G_{\rm ind}({\bf x},{\bf x}')$  directly proportional to eq 1 by a factor of charge, q. The coordinates  $Q_{lm} \equiv Q_{lm}(t)$  of the multipole plasmons in the spherical basis 45 can be projected onto their Cartesian analogues. 61 The corner modes of the nanocube are each approximated as a single Cartesian plasmon coordinate, leading directly to the definition of the free-space plasmon Hamiltonian. The interactions between the corner modes are limited by symmetry, with  $H_{\rm int}$  determining the self-coupling constants

$$f_{i} = \frac{2e^{2}\Delta_{21}}{m_{i}\varepsilon_{b}(2a)^{3}} - \sum_{j=1}^{\infty} \frac{2e^{2}\Delta_{23}[1 - \Delta_{21}^{2}](\Delta_{21}\Delta_{23})^{j-1}}{m_{i}\varepsilon_{b}(2a + 2jt)^{3}}$$

$$f_{z} = \frac{4e^{2}\Delta_{21}}{m_{z}\varepsilon_{b}(2a)^{3}} - \sum_{j=1}^{\infty} \frac{4e^{2}\Delta_{23}[1 - \Delta_{21}^{2}](\Delta_{21}\Delta_{23})^{j-1}}{m_{z}\varepsilon_{b}(2a + 2jt)^{3}}$$

$$f_{xy} = \frac{4}{3}\frac{e^{2}a^{2}\Delta_{21}}{m_{xy}\varepsilon_{b}(2a)^{5}} - \sum_{j=1}^{\infty} \frac{4}{3}\frac{e^{2}a^{2}\Delta_{23}[1 - \Delta_{21}^{2}](\Delta_{21}\Delta_{23})^{j-1}}{m_{xy}\varepsilon_{b}(2a + 2jt)^{5}}$$

$$f_{iz} = \frac{12e^{2}a^{2}\Delta_{21}}{m_{iz}\varepsilon_{b}(2a)^{5}} - \sum_{j=1}^{\infty} \frac{12e^{2}a^{2}\Delta_{23}[1 - \Delta_{21}^{2}](\Delta_{21}\Delta_{23})^{j-1}}{m_{iz}\varepsilon_{b}(2a + 2jt)^{5}}$$

$$f_{xyz} = \frac{16e^{2}a^{4}\Delta_{21}}{m_{xyz}\varepsilon_{b}(2a)^{7}} - \sum_{j=1}^{\infty} \frac{16e^{2}a^{4}\Delta_{23}[1 - \Delta_{21}^{2}](\Delta_{21}\Delta_{23})^{j-1}}{m_{xyz}\varepsilon_{b}(2a + 2jt)^{7}}$$

$$(7)$$

and cross-coupling constants

$$g_{i} = \frac{e^{2}a\Delta_{21}}{\sqrt{m_{i}m_{iz}}} \varepsilon_{b}(2a)^{4} - \sum_{j=1}^{\infty} \frac{e^{2}a\Delta_{23}[1 - \Delta_{21}^{2}](\Delta_{21}\Delta_{23})^{j-1}}{\sqrt{m_{i}m_{iz}}} \varepsilon_{b}(2a + 2jt)^{4}$$

$$g_{xy} = \frac{e^{2}a^{3}\Delta_{21}}{\sqrt{m_{xy}m_{xyz}}} \varepsilon_{b}(2a)^{6} - \sum_{j=1}^{\infty} \frac{e^{2}a^{3}\Delta_{23}[1 - \Delta_{21}^{2}](\Delta_{21}\Delta_{23})^{j-1}}{\sqrt{m_{xy}m_{xyz}}} \varepsilon_{b}(2a + 2jt)^{6}}$$
(8)

for  $i \in \{x, y\}$ . Each coupling constant, here derived in the case of the nanosphere on a finite substrate, is scaled to reproduce the EEL spectrum of the nanocube on a finite substrate. In general, the nanocube's (corner mode) coupling constants are larger than those of the nanosphere, implying that the nanocube couples more readily to the substrate than the nanosphere.

Diagonalization of the total Hamiltonian produces the hybridized LSP modes and frequencies defined in the text.

EELS Simulations. Simulations were performed using both the electron-driven discrete dipole approximation (e-DDA)<sup>62,63</sup> and the metal nanoparticle boundary element method (MNPBEM14).<sup>64</sup> In these codes, a nanoparticle's volume or boundary surfaces are divided into a collection of discrete elements that are polarized by an external field as well by each other. Using a plane wave and an electron beam as a source, scattering and EEL spectra were calculated. The electron beam was given an initial energy of 200 keV and an impact parameter of 0.5 nm from the specified proximal or distal corner of the cube. As was done experimentally, EEL maps were calculated by filtering the EEL spectra acquired within a region of interest surrounding the target at a specific loss energy value.

## AUTHOR INFORMATION

## **Corresponding Authors**

\*E-mail: jon.camden@nd.edu.

\*E-mail: masiello@chem.washington.edu.

#### ORCID ®

Jon P. Camden: 0000-0002-6179-2692 David J. Masiello: 0000-0002-1187-0920

### **Author Contributions**

Contributed equally to this work

#### Notes

The authors declare no competing financial interest.

### ACKNOWLEDGMENTS

This work was supported by the University of Washington, the University of Notre Dame, the U.S. Department of Energy Basic Energy Sciences under Award Number DE-SC0018040 (D.J.M., J.P.C.), and the U.S. National Science Foundation under Grant Number DMR-1708189 (D.J.M., J.P.C.). G.L. also acknowledges support from a Notre Dame Energy postdoctoral fellowship. This work was facilitated though the use of advanced computational, storage, and networking infrastructure provided by the Hyak supercomputer system at the University of Washington. G.L. and J.P.C. thank the imaging facility at the University of Tennessee Knoxville for assistance with and access to the Zeiss Libra STEM.

## REFERENCES

- (1) Willets, K. A.; Van Duyne, R. P. Localized Surface Plasmon Resonance Spectroscopy and Sensing. *Annu. Rev. Phys. Chem.* **2007**, *58*, 267–297.
- (2) Atwater, H. A.; Polman, A. Plasmonics for Improved Photovoltaic Devices. *Nat. Mater.* **2010**, *9*, 205–213.
- (3) Unser, S.; Bruzas, I.; He, J.; Sagle, L. Localized Surface Plasmon Resonance Biosensing: Current Challenges and Approaches. *Sensors* **2015**, *15*, 15684–15716.
- (4) Brongersma, M. L.; Halas, N. J.; Nordlander, P. Plasmon-Induced Hot Carrier Science and Technology. *Nat. Nanotechnol.* **2015**, *10*, 25–34
- (5) Wang, J.; Zhang, H. Z.; Li, R. S.; Huang, C. Z. Localized Surface Plasmon Resonance of Gold Nanorods and Assemblies in the View of Biomedical Analysis. *TrAC, Trends Anal. Chem.* **2016**, *80*, 429–443.
- (6) Baffou, G.; Quidant, R. Thermo-Plasmonics: Using Metallic Nanostructures as Nano-Sources of Heat. *Laser Photonics Rev.* **2013**, *7*, 171–187.
- (7) Luk'yanchuk, B.; Zheludev, N. I.; Maier, S. A.; Halas, N. J.; Nordlander, P.; Giessen, H.; Chong, C. T. The Fano Resonance in Plasmonic Nanostructures and Metamaterials. *Nat. Mater.* **2010**, *9*, 707–715.

- (8) Zhang, X.; Chen, Y. L.; Liu, R.-S.; Tsai, D. P. Plasmonic Photocatalysis. *Rep. Prog. Phys.* **2013**, *76*, 046401.
- (9) Tang, L.; Casas, J.; Venkataramasubramani, M. Magnetic Nanoparticle Mediated Enhancement of Localized Surface Plasmon Resonance for Ultrasensitive Bioanalytical Assay in Human Blood Plasma. *Anal. Chem.* **2013**, *85*, 1431–1439.
- (10) Singh, M. P.; Strouse, G. F. Involvement of the LSPR Spectral Overlap for Energy Transfer Between a Dye and Au Nanoparticle. *J. Am. Chem. Soc.* **2010**, *132*, 9383–9391.
- (11) Zhao, J.; Zhang, X.; Yonzon, C. R.; Haes, A. J.; Van Duyne, R. P. Localized Surface Plasmon Resonance Biosensors. *Nanomedicine* **2006**, *1*, 219–228.
- (12) Cao, J.; Sun, T.; Grattan, K. T. Gold Nanorod-Based Localized Surface Plasmon Resonance Biosensors: A Review. *Sens. Actuators, B* **2014**, *195*, 332–351.
- (13) Huang, H.; Zhang, L.; Lv, Z.; Long, R.; Zhang, C.; Lin, Y.; Wei, K.; Wang, C.; Chen, L.; Li, Z.-Y.; et al. Unraveling Surface Plasmon Decay in Core-Shell Nanostructures toward Broadband Light-Driven Catalytic Organic Synthesis. J. Am. Chem. Soc. 2016, 138, 6822–6828.
- (14) Li, J.; Cushing, S. K.; Zheng, P.; Meng, F.; Chu, D.; Wu, N. Plasmon-Induced Photonic and Energy-Transfer Enhancement of Solar Water Splitting by a Hematite Nanorod Array. *Nat. Commun.* **2013**, *4*, 2651
- (15) Li, K.; Hogan, N. J.; Kale, M. J.; Halas, N. J.; Nordlander, P.; Christopher, P. Balancing Near-Field Enhancement, Absorption, and Scattering for Effective Antenna-Reactor Plasmonic Photocatalysis. *Nano Lett.* **2017**, *17*, 3710–3717.
- (16) Swearer, D. F.; Zhao, H.; Zhou, L.; Zhang, C.; Robatjazi, H.; Martirez, J. M. P.; Krauter, C. M.; Yazdi, S.; McClain, M. J.; Ringe, E.; et al. Heterometallic Antenna- Reactor Complexes for Photocatalysis. *Proc. Natl. Acad. Sci. U. S. A.* **2016**, *113*, 8916–8920.
- (17) Chang, W.-S.; Ha, J. W.; Slaughter, L. S.; Link, S. Plasmonic Nanorod Absorbers as Orientation Sensors. *Proc. Natl. Acad. Sci. U. S. A.* **2010**, *107*, 2781–2786.
- (18) Lassiter, J. B.; Sobhani, H.; Fan, J. A.; Kundu, J.; Capasso, F.; Nordlander, P.; Halas, N. J. Fano Resonances in Plasmonic Nanoclusters: Geometrical and Chemical Tunability. *Nano Lett.* **2010**, *10*, 3184–3189.
- (19) Gallinet, B.; Martin, O. J. Refractive Index Sensing with Subradiant Modes: A Framework to Reduce Losses in Plasmonic Nanostructures. *ACS Nano* **2013**, *7*, 6978–6987.
- (20) Kreibig, U.; Vollmer, M. Optical Poperties of Metal Clusters; Springer Series in Materials Science; Springer-Verlag: New York, 1995; Vol. 25.
- (21) Evanoff, D. D.; Chumanov, G. Size-controlled synthesis of nanoparticles. 2. Measurement of extinction, scattering, and absorption cross sections. *J. Phys. Chem. B* **2004**, *108*, 13957–13962.
- (22) Maier, S. A. Effective mode volume of nanoscale plasmon cavities. *Opt. Quantum Electron.* **2006**, 38, 257–267.
- (23) Sauvan, C.; Hugonin, J.-P.; Maksymov, I.; Lalanne, P. Theory of the spontaneous optical emission of nanosize photonic and plasmon resonators. *Phys. Rev. Lett.* **2013**, *110*, 237401.
- (24) Chang, D.; Sørensen, A. S.; Hemmer, P.; Lukin, M. Quantum optics with surface plasmons. *Phys. Rev. Lett.* **2006**, *97*, 053002.
- (25) Catchpole, K.; Polman, A. Design principles for particle plasmon enhanced solar cells. *Appl. Phys. Lett.* **2008**, 93, 191113.
- (26) Hagfeldt, A.; Boschloo, G.; Sun, L.; Kloo, L.; Pettersson, H. Dyesensitized solar cells. *Chem. Rev.* **2010**, *110*, 6595–6663.
- (27) Wu, D. M.; García-Etxarri, A.; Salleo, A.; Dionne, J. A. Plasmonenhanced upconversion. *J. Phys. Chem. Lett.* **2014**, *5*, 4020–4031.
- (28) Heylman, K. D.; Thakkar, N.; Horak, E. H.; Quillin, S. C.; Cherqui, C.; Knapper, K. A.; Masiello, D. J.; Goldsmith, R. H. Optical microresonators as single-particle absorption spectrometers. *Nat. Photonics* **2016**, *10*, 788–795.
- (29) Thakkar, N.; Rea, M. T.; Smith, K. C.; Heylman, K. D.; Quillin, S. C.; Knapper, K. A.; Horak, E. H.; Masiello, D. J.; Goldsmith, R. H. Sculpting Fano Resonances To Control Photonic—Plasmonic Hybridization. *Nano Lett.* **2017**, *17*, 6927—6934.

- (30) Cherqui, C.; Wu, Y.; Li, G.; Quillin, S. C.; Busche, J. A.; Thakkar, N.; West, C. A.; Montoni, N. P.; Rack, P. D.; Camden, J. P.; et al. STEM/EELS Imaging of Magnetic Hybridization in Symmetric and Symmetry-Broken Plasmon Oligomer Dimers and All-Magnetic Fano Interference. *Nano Lett.* **2016**, *16*, 6668–6676. PMID: 27673696.
- (31) Pendry, J. B.; Holden, A.; Stewart, W.; Youngs, I. Extremely low frequency plasmons in metallic mesostructures. *Phys. Rev. Lett.* **1996**, *76*, 4773
- (32) García de Abajo, F. J. Nonlocal effects in the plasmons of strongly interacting nanoparticles, dimers, and waveguides. *J. Phys. Chem. C* **2008**, *112*, 17983–17987.
- (33) Toudert, J.; Simonot, L.; Camelio, S.; Babonneau, D. Advanced optical effective medium modeling for a single layer of polydisperse ellipsoidal nanoparticles embedded in a homogeneous dielectric medium: surface plasmon resonances. *Phys. Rev. B: Condens. Matter Mater. Phys.* **2012**, *86*, 045415.
- (34) Berini, P. Plasmon-polariton modes guided by a metal film of finite width bounded by different dielectrics. *Opt. Express* **2000**, *7*, 329–335
- (35) Spinelli, P.; Hebbink, M.; De Waele, R.; Black, L.; Lenzmann, F.; Polman, A. Optical impedance matching using coupled plasmonic nanoparticle arrays. *Nano Lett.* **2011**, *11*, 1760–1765.
- (36) Royer, P.; Goudonnet, J.; Warmack, R.; Ferrell, T. Substrate effects on surface-plasmon spectra in metal-island films. *Phys. Rev. B: Condens. Matter Mater. Phys.* 1987, 35, 3753.
- (37) Zhang, S.; Bao, K.; Halas, N. J.; Xu, H.; Nordlander, P. Substrate-Induced Fano Resonances of a Plasmonic Nanocube: A Route to Increased-Sensitivity Localized Surface Plasmon Resonance Sensors Revealed. *Nano Lett.* **2011**, *11*, 1657–1663.
- (38) Wu, Y.; Li, G.; Cherqui, C.; Bigelow, N. W.; Thakkar, N.; Masiello, D. J.; Camden, J. P.; Rack, P. D. Electron Energy Loss Spectroscopy Study of the Full Plasmonic Spectrum of Self-Assembled Au-Ag Alloy Nanoparticles: Unraveling Size, Composition, and Substrate Effects. *ACS Photonics* **2016**, *3*, 130–138.
- (39) Li, G.; Cherqui, C.; Wu, Y.; Bigelow, N. W.; Simmons, P. D.; Rack, P. D.; Masiello, D. J.; Camden, J. P. Examining substrate-induced plasmon mode splitting and localization in truncated silver nanospheres with electron energy loss spectroscopy. *J. Phys. Chem. Lett.* **2015**, *6*, 2569–2576.
- (40) Li, G.; Cherqui, C.; Bigelow, N. W.; Duscher, G.; Straney, P. J.; Millstone, J. E.; Masiello, D. J.; Camden, J. P. Spatially Mapping Energy Transfer from Single Plasmonic Particles to Semiconductor Substrates via STEM/EELS. *Nano Lett.* **2015**, *15*, 3465–3471.
- (41) Beck, F.; Polman, A.; Catchpole, K. Tunable light trapping for solar cells using localized surface plasmons. *J. Appl. Phys.* **2009**, *105*, 114310
- (42) Ritchie, R. Plasma losses by fast electrons in thin films. *Phys. Rev.* **1957**, *106*, 874.
- (43) Stern, E.; Ferrell, R. Surface plasma oscillations of a degenerate electron gas. *Phys. Rev.* **1960**, *120*, 130.
- (44) García de Abajo, F. J. Optical excitations in electron microscopy. *Rev. Mod. Phys.* **2010**, 82, 209.
- (45) Cherqui, C.; Thakkar, N.; Li, G.; Camden, J. P.; Masiello, D. J. Characterizing Localized Surface Plasmons Using Electron Energy-Loss Spectroscopy. *Annu. Rev. Phys. Chem.* **2016**, *67*, 331–357.
- (46) Wu, Y.; Li, G.; Camden, J. P. Probing Nanoparticle Plasmons with Electron Energy Loss Spectroscopy. *Chem. Rev.* **2017**, DOI: 10.1021/acs.chemrev.7b00354.
- (47) Cahill, K. Models of membrane electrostatics. *Phys. Rev. E* **2012**, 85, 051921.
- (48) Sherry, L. J.; Chang, S. H.; Schatz, G. C.; Van Duyne, R. P.; Wiley, B. J.; Xia, Y. N. Localized surface plasmon resonance spectroscopy of single silver nanocubes. *Nano Lett.* **2005**, *5*, 2034–2038.
- (49) Nicoletti, O.; de La Peña, F.; Leary, R. K.; Holland, D. J.; Ducati, C.; Midgley, P. A. Three-Dimensional Imaging of Localized Surface Plasmon Resonances of Metal Nanoparticles. *Nature* **2013**, *502*, 80–84. (50) Mazzucco, S.; Geuquet, N.; Ye, J.; Stéphan, O.; Van Roy, W.; Van

Dorpe, P.; Henrard, L.; Kociak, M. Ultralocal Modification of Surface

- Plasmons Properties in Silver Nanocubes. Nano Lett. 2012, 12, 1288–1294
- (51) Akselrod, G. M.; Argyropoulos, C.; Hoang, T. B.; Ciraci, C.; Fang, C.; Huang, J.; Smith, D. R.; Mikkelsen, M. H. Probing the mechanisms of large Purcell enhancement in plasmonic nanoantennas. *Nat. Photonics* **2014**, *8*, 835–840.
- (52) Dill, T. J.; Rozin, M. J.; Palani, S.; Tao, A. R. Colloidal Nanoantennas for Hyperspectral Chemical Mapping. *ACS Nano* **2016**, 10, 7523–7531.
- (53) Saito, K.; Tatsuma, T. Asymmetric Three-Way Plasmonic Color Routers. *Adv. Opt. Mater.* **2015**, *3*, 883–887.
- (54) Saito, K.; Tatsuma, T. A Transparent Projection Screen Based on Plasmonic Ag Nanocubes. *Nanoscale* **2015**, *7*, 20365–20368.
- (55) Hoang, T. B.; Akselrod, G. M.; Argyropoulos, C.; Huang, J.; Smith, D. R.; Mikkelsen, M. H. Ultrafast Spontaneous Emission Source Using Plasmonic Nanoantennas. *Nat. Commun.* **2015**, *6*, 7788.
- (56) Kawawaki, T.; Wang, H.; Kubo, T.; Saito, K.; Nakazaki, J.; Segawa, H.; Tatsuma, T. Efficiency enhancement of PbS quantum Dot/ZnO nanowire bulk-heterojunction solar cells by plasmonic silver nanocubes. *ACS Nano* **2015**, *9*, 4165–4172.
- (57) Baek, S.-W.; Park, G.; Noh, J.; Cho, C.; Lee, C.-H.; Seo, M.-K.; Song, H.; Lee, J.-Y. Au@Ag core-shell nanocubes for efficient plasmonic light scattering effect in low bandgap organic solar cells. *ACS Nano* **2014**, 8, 3302–3312.
- (58) Li, J.; Cushing, S. K.; Meng, F.; Senty, T. R.; Bristow, A. D.; Wu, N. Plasmon-induced resonance energy transfer for solar energy conversion. *Nat. Photonics* **2015**, *9*, 601–607.
- (59) Hoggard, A.; Wang, L.-Y.; Ma, L.; Fang, Y.; You, G.; Olson, J.; Liu, Z.; Chang, W.-S.; Ajayan, P. M.; Link, S. Using the Plasmon Linewidth To Calculate the Time and Efficiency of Electron Transfer between Gold Nanorods and Graphene. *ACS Nano* **2013**, *7*, 11209–11217.
- (60) Busche, J. A.; Cherqui, C.; Li, G.; Camden, J. P.; Masiello, D. J. In Preparation.
- (61) Milton, K.; Schwinger, J. Electromagnetic Radiation: Variational Methods, Waveguides and Accelerators; Particle Acceleration and Detection; Springer: Berlin Heidelberg, 2006.
- (62) Bigelow, N. W.; Vaschillo, A.; Iberi, V.; Camden, J. P.; Masiello, D. J. Characterization of the Electron- and Photon-Driven Plasmonic Excitations of Metal Nanorods. *ACS Nano* **2012**, *6*, 7497–7504.
- (63) Bigelow, N. W.; Vaschillo, A.; Camden, J. P.; Masiello, D. J. Signatures of Fano Interferences in the Electron Energy Loss Spectroscopy and Cathodoluminescence of Symmetry-Broken Nanorod Dimers. *ACS Nano* **2013**, *7*, 4511–4519.
- (64) Hohenester, U.; Trügler, A. MNPBEM—A Matlab toolbox for the simulation of plasmonic nanoparticles. *Comput. Phys. Commun.* **2012**, 183, 370—381.